Biomedical Optics EXPRESS

Vibrationally resonant sum-frequency generation microscopy with a solid immersion lens

Eun Seong Lee,[1] Sang-Won Lee,[2] Julie Hsu,[3] and Eric O. Potma[3,*]

[1]*Center for Nanometrology, Korea Research Institute of Standards and Science, 267 Gajeong-ro, Yuseong-gu, Daejeon 304-340, South Korea*

[2]*Center for NanoSafety, Korea Research Institute of Standards and Science, 267 Gajeong-ro, Yuseong-gu, Daejeon 304-340, South Korea*

[3]*Beckman Laser Institute, University of California, Irvine, California 92697, USA*

[*]*epotma@uci.edu*

Abstract: We use a hemispheric sapphire lens in combination with an off-axis parabolic mirror to demonstrate high-resolution vibrationally resonant sum-frequency generation (VR-SFG) microscopy in the mid-infrared range. With the sapphire lens as an immersed solid medium, the numerical aperture (NA) of the parabolic mirror objective is enhanced by a factor of 1.72, from 0.42 to 0.72, close to the theoretical value of 1.76 (= $n_{sapphire}$). The measured lateral resolution is as high as 0.64 μm. We show the practical utility of the sapphire immersion lens by imaging collagen-rich tissues with and without the solid immersion lens.

OCIS codes: (170.0180) Microscopy; (180.4315) Nonlinear microscopy; (190.4223) Nonlinear wave mixing; (110.3080) Infrared imaging.

References and links

1. B. C. Smith, *Fundamentals of Fourier Transform Infrared Spectroscopy* (CRC Press, Boca Raton, 2011).
2. F. Garczarek and K. Gerwert, "Functional waters in intraprotein proton transfer monitored by FTIR difference spectroscopy," Nature **439**(7072), 109–112 (2006).
3. R. Mendelsohn, H. C. Chen, M. E. Rerek, and D. J. Moore, "Infrared microspectroscopic imaging maps the spatial distribution of exogenous molecules in skin," J. Biomed. Opt. **8**(2), 185–190 (2003).
4. K. Inoue, N. Bokor, S. Kogure, M. Fujii, and M. Sakai, "Two-point-separation in a sub-micron nonscanning IR super-resolution microscope based on transient fluorescence detected IR spectroscopy," Opt. Express **17**(14), 12013–12018 (2009).
5. E. S. Lee and J. Y. Lee, "High resolution cellular imaging with nonlinear optical infrared microscopy," Opt. Express **19**(2), 1378–1384 (2011).
6. V. Raghunathan, Y. Han, O. Korth, N. H. Ge, and E. O. Potma, "Rapid vibrational imaging with sum frequency generation microscopy," Opt. Lett. **36**(19), 3891–3893 (2011).
7. Y. Han, V. Raghunathan, R. R. Feng, H. Maekawa, C. Y. Chung, Y. Feng, E. O. Potma, and N. H. Ge, "Mapping molecular orientation with phase sensitive vibrationally resonant sum-frequency generation microscopy," J. Phys. Chem. B **117**(20), 6149–6156 (2013).
8. M. Flörsheimer, C. Brillert, and H. Fuchs, "Chemical imaging of interfaces by sum frequency microscopy," Langmuir **15**(17), 5437–5439 (1999).
9. K. Kuhnke, D. M. P. Hoffmann, X. C. Wu, A. M. Bittner, and K. Kern, "Chemical imaging of interfaces by sum-frequency generation microscopy: application to patterned self-assembled monolayers," Appl. Phys. Lett. **83**(18), 3830–3832 (2003).
10. K. A. Cimatu and S. Baldelli, "Chemical microscopy of surfaces by sum frequency generation imaging," J. Phys. Chem. C **113**(38), 16575–16588 (2009).
11. H. C. Hieu, N. A. Tuan, H. Li, Y. Miyauchi, and G. Mizutani, "Sum frequency generation microscopy study of cellulose fibers," Appl. Spectrosc. **65**(11), 1254–1259 (2011).
12. J. H. Jang, J. Jacob, G. Santos, T. R. Lee, and S. Baldelli, "Image contrast in sum-frequency generation microscopy based on monolayer order and coverage," J. Phys. Chem. C **117**(29), 15192–15202 (2013).
13. D. S. Grey, "A new series of microscope objectives; Preliminary investigation of catadioptric Schwarzschild systems," J. Opt. Soc. Am. **39**(9), 723–728 (1949).
14. S. T. Yang, R. L. Hsieh, Y. H. Lee, R. F. W. Pease, and G. Owen, "Effect of central obscuration on image formation in projection lithography," Proc. SPIE **1264**, 477–485 (1990).
15. N. Olivier, D. DéBarre, P. Mahou, and E. Beaurepaire, "Third-harmonic generation microscopy with Bessel beams: a numerical study," Opt. Express **20**(22), 24886–24902 (2012).

#209910 - $15.00 USD Received 9 Apr 2014; revised 21 May 2014; accepted 21 May 2014; published 9 Jun 2014

16. S. M. Mansfield and G. S. Kino, "Solid immersion microscope," Appl. Phys. Lett. **57**(24), 2615–2616 (1990).
17. L. P. Ghislain and V. B. Elings, "Near-field scanning solid immersion microscope," Appl. Phys. Lett. **72**(22), 2779–2781 (1998).
18. Q. Wu, R. D. Grober, D. Gammon, and D. S. Katzer, "Imaging spectroscopy of two-dimensional excitons in a narrow GaAs/AlGaAs quantum well," Phys. Rev. Lett. **83**(13), 2652–2655 (1999).
19. Q. Wu, G. D. Feke, R. D. Grober, and L. P. Ghislain, "Realization of numerical aperture 2.0 using a gallium phosphide solid immersion lens," Appl. Phys. Lett. **75**(26), 4064–4066 (1999).
20. D. A. Fletcher, K. B. Crozier, C. F. Quate, G. S. Kino, K. E. Goodson, D. Simanovskii, and D. V. Palanker, "Near-field infrared imaging with a microfabricated solid immersion lens," Appl. Phys. Lett. **77**(14), 2109–2111 (2000).
21. S. B. Ippolito, B. B. Goldberg, and M. S. Unlu, "High spatial resolution subsurface microscopy," Appl. Phys. Lett. **78**(26), 4071–4073 (2001).
22. K. Cohn, D. Simanovskii, T. Smith, and D. Palanker, "Transient photoinduced diffractive solid immersion lens for infrared microscopy," Appl. Phys. Lett. **81**(19), 3678–3680 (2002).
23. B. D. Terris, H. J. Mamin, and D. Rugar, "Near-field optical data storage," Appl. Phys. Lett. **68**(2), 141–143 (1996).
24. T. D. Milster, "Near-field optical data storage: avenues for improved performance," Opt. Eng. **40**(10), 2255–2260 (2001).
25. Y. Lu, J. Xie, J. Jhang, H. Ming, and P. Wang, "Increased the storage density of solid immersion lens system by high-pass angular spectrum filter method," Opt. Commun. **203**(1-2), 87–92 (2002).
26. T. S. Song, H. D. Kwon, Y. J. Yoon, K. S. Jung, N. C. Park, and Y. P. Park, "Aspherical solid immersion lens of integrated optical head for near-field recording," Jpn. J. Appl. Phys. **42**(Part 1, No. 2B), 1082–1089 (2003).
27. M. K. Hong, A. G. Jeung, N. V. Dokholyan, T. I. Smith, H. A. Schwettman, P. Huie, and S. Erramilli, "Imaging single living cells with a scanning near-field infrared microscope based on a free electron laser," Nucl. Instrum. Methods Phys. Res. B **144**(1-4), 246–255 (1998).
28. M. Baba, T. Sasaki, M. Yoshita, and H. Akiyama, "Aberrations and allowances for errors in a hemisphere solid immersion lens for submicron-resolution photoluminescence microscopy," J. Appl. Phys. **85**(9), 6923–6925 (1999).

1. Introduction

Optical microscopy with mid-infrared (MIR; 2.5-25 μm) light enables spectroscopic imaging with contrast based on molecular vibrational modes. Several linear and nonlinear optical imaging techniques with vibrational contrast have been developed for biological applications in the MIR region with high sensitivity [1–7]. Among these, vibrationally resonant sum-frequency generation (VR-SFG) microscopy is a second-order nonlinear optical imaging technique, which is sensitive to samples with noncentrosymmetry [6–12]. VR-SFG is suitable for imaging biopolymers with a nonvanishing second-order susceptibility $\chi^{(2)}$, such as collagen, microtubules and cellulose. The molecular modes in VR-SFG are excited with an optical frequency ω_1 in the MIR range, followed by an upconversion with a second optical frequency ω_2 in the visible/near-infrared range to generate a visible signal at $\omega_1 + \omega_2$. Since $\chi^{(2)}$ is frequency dependent in the MIR range, the signal grows stronger when the ω_1 frequency approaches resonances of SFG-active molecular vibrational modes.

An attractive feature of objective-based VR-SFG microscopy is that it enables MIR-based imaging with a spatial resolution well below a micrometer, as the size of the probing volume is defined by the product of the MIR and the visible/NIR excitation spots [6,7]. In addition, the visible signal can be efficiently captured with standard optics and detected with sensitive photodetectors in the visible range. Nonetheless, the VR-SFG resolution is inferior to that of conventional forms of optical microscopy, because the high numerical aperture (NA) refractive objectives that are commonly used in the visible/NIR region are incompatible with MIR excitation light. Objective-based VR-SFG microscopy has been achieved with all-reflective objectives such as Schwarzschild-type lenses [6,7]. Although Schwarzschild lenses are commercially available, their maximum NA is presently 0.65, which is well below the NA of standard refractive objectives. Moreover, the Schwarzschild objective features a central obscuration that affects the shape and size of the focal volume compared to refractive objectives [13,14]. The central obscuration produces a point-spread function that exhibits more pronounced diffraction side lobes in the lateral dimension, and an elongated profile in the axial dimension. These unwanted properties of the focal excitation fields produce distorted images, result in exceptionally poor axial resolution and give rise to inefficient nonlinear signal generation [15].

#209910 - $15.00 USD Received 9 Apr 2014; revised 21 May 2014; accepted 21 May 2014; published 9 Jun 2014

Evidently, these complications have prevented VR-SFG microscopy to reach its full potential. Alternative excitation schemes that improve the quality of the focal volume are highly desirable. In this work, we make an important step towards improving the imaging performance of the VR-SFG microscope. Our scheme is based on the use of an all-reflective off-axis parabolic mirror of short focal length and wide aperture. To further enhance the focusing capability of the parabolic mirror, we implement a solid immersion lens (SIL) method, where the high refractive index of the lens material increases the effective NA of the focusing system [16–22]. The SIL technology has been previously used in optical pickup devices to increase the data density of optical data storage systems [23–26]. Here we implement an off-the-shelf, hemispheric sapphire SIL for simultaneously focusing MIR and NIR to demonstrate high-resolution VR-SFG imaging with an effective NA of 0.72. We show that this simple and cost-effective solution produces high quality SFG images of collagen-rich biological tissues such as tendon and cornea.

2. Experimental setup

The basic optical layout of the VR-SFG microscope along with a depiction of the sapphire hemispheric SIL (Edmund Optics, diameter 6.35 mm) is shown in Fig. 1. The SFG excitation scheme is based on our previous report [6], where tunable MIR and a NIR pulse trains (6 ps pulse width, 76 MHz repetition rate) generated from an optical parametric oscillator (Levante OPO, APE Berlin) are combined on a dichroic mirror in a collinear fashion as shown in Fig. 1. The beams subsequently pass through an all-reflective telescope, which consists of two off-axis parabolic mirrors (ThorLabs Inc., effective focal length = 25.4 mm and 203.2 mm). After the telescope, the beam diameter is about 25 mm. The distance between the two parabolic mirrors is made adjustable to obtain an exact confocal geometry. The latter is important for minimizing the aberration arising from a non-perfect confocality, which may introduce distortions to the excitation volume in the focal plane. The achromaticity of the all-reflective telescope is a significant advantage for our SFG experiments relative to refractive optics. Since the incident frequencies ω_1 and ω_2 are notably different, optimization of achromaticity is essential for achieving acceptable imaging properties of the VR-SFG microscope.

Before focusing, the ω_1 and ω_2 beams are linearly polarized in parallel fashion. The expanded beams are incident on a short focal length off-axis parabolic mirror (Edmund Optics, focal length = 25.4 mm), which acts as an objective lens and forms a focal spot in the sample. When the aperture of the mirror is filled, the effective NA of the focusing element is 0.42. The sapphire SIL is placed above the parabolic mirror in such a way that the focal point is just above the SIL flat surface, as illustrated in Fig. 1. To do so, we observe the partially reflected beam from the SIL spherical surface and retrace it to the incoming beam path. The MIR wavelength was tuned to 3.4 μm (2945 cm^{-1}) corresponding to the methylene mode of collagen, and the associated NIR beam was set at 775 nm. The samples are put on the SIL surface and raster-scanned using a two-axis piezo translation stage for generating 2D images. The SFG signal is detected in the forward propagation direction by a photomultiplier tube (PMT) via the condenser lens and a 632 ± 22 nm bandpass filter.

#209910 - $15.00 USD Received 9 Apr 2014; revised 21 May 2014; accepted 21 May 2014; published 9 Jun 2014

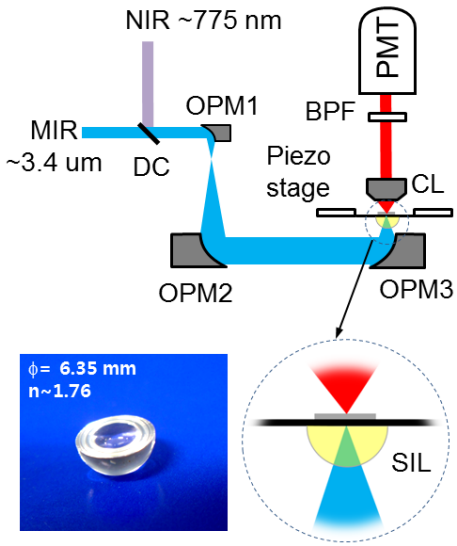

Fig. 1. Experimental setup of solid immersion VR-SFG microscope. The collinearly overlapped MIR and NIR beams generate the sum frequency signal at 631.1 nm from the sample on the piezo stage. The hemispherical sapphire SIL is combined with the off-axis parabolic mirror (OPM3) to increase the system NA by a factor of $n_{sapphire}$ (= 1.76). A lateral FWHM of 0.64 μm for the focal excitation volume is achieved in the present setup. OPM, off-axis parabolic mirror; SIL, solid immersion lens; DC, dichroic mirror; BPF, bandpass filter; CL, condenser lens; PMT, photomultiplier tube.

3. Ray tracing through the sapphire SIL

To optimize the experimental layout, we perform ray tracing and point spread function (PSF) simulations using commercial software (ZEMAX) for modeling the performance of the sapphire SIL in combination with the off-axis parabolic mirror. To model the effect of the reflective mirrors, we assume that the radiation after the last focusing mirror can be described as a perfect converging spherical wavefront, which is incident on the SIL. After passing through the SIL, the light propagates into the water medium, which closely mimics the experimental situation. The refractive indices of sapphire used in the simulations are 1.76 and 1.70 at the wavelengths 775 nm and 3.4 μm respectively, while those of water are 1.33 and 1.42 respectively. The diameter of the hemispheric SIL is 6.35 mm. Only the ordinary wave for birefringent sapphire is considered here. Because the polarization of incident laser beams can be adjusted precisely to either orientation in actual experiments, and the refractive index difference is less than 0.5% between two polarizations, the assumption of one ordinary index value is appropriate.

The ray tracing and focal intensity calculation results for three cases are shown in Fig. 2. Figure 2(a) represents the focusing beam from the parabolic mirror (at the bottom; not shown) with an effective NA 0.42 without SIL, where the wavelength is set to 775 nm. The beam is focused onto the air-water interface and produces a diffraction-limited spot, as shown in Fig. 2(d). The full-width at half-maximum (FWHM) of the spot is 1.07 μm. Figure 2(b) and 2(e) show the corresponding results with the SIL inserted. The FWHM at the flat SIL surface is reduced by $n_{sapphire}$ ($n_{sapphire}$ = refractive index of sapphire, 1.76) to provide a focal spot with a width of 0.61 μm; a direct manifestation of the increased NA. These results model the situation relevant to SIL focusing in optical pickup applications, where the evanescent field within ~200 nm from SIL surface plays an important role in reducing the focal spot size relative to the focus formed through free-space diffraction. In the present study, however, because the incident converging angle is below the critical angle at the sapphire-water interface, no evanescent field is generated. This implies that focusing with an increased effective NA is not limited to the region near the interface, but can instead be achieved deeper

#209910 - $15.00 USD Received 9 Apr 2014; revised 21 May 2014; accepted 21 May 2014; published 9 Jun 2014

into the water medium. Figure 2(c) shows the case in which the focal point is placed 10 μm above the SIL surface. Figure 2(f) shows that the FWHM of the focal intensity in this case is comparable to the situation in Fig. 2(e). The result is intriguing in that high-resolution imaging is still possible for objects placed away from the SIL surface.

To model the situation of deeper focusing in Fig. 2(c), we decrease the distance between parabolic mirror and SIL by 20 μm to raise the focus above the SIL surface. We find that the reduced FWHM persists up to ~20 μm from the SIL surface. Beyond this distance, spherical aberration starts to become more significant, which broadens the focal volume. The 20 μm range is relevant for the present study because the penetration depth of water is around 10 μm in the MIR region of interest [27]. The PSF calculation results for the MIR excitation wavelength of 3.4 μm are shown in Fig. 2(g)-2(i) for similar scenarios. We note that as the focal point is removed farther away from the SIL surface (as in Fig. 2(c)), chromatic aberrations in the sapphire material grow more significant. The refractive index difference between the 775 nm and 3.4 μm excitation wavelengths amounts to 3.4%, which introduces a small chromatic focal shift of ~1.2 μm when focusing 10 μm deep into the sample. This chromatic focal shift is small compared to the axial extent of the focal volume, which amounts to 3.5 μm FWHM at a focusing depth of 10 μm.

An important advantage of the current configuration is the lack of a central obscuration in the focusing geometry. To illustrate this point, we have performed calculations of the axial FWHM at the focusing depth of 10 μm when the central portion of the incident beam is blocked by an opaque pupil. We find that, if the pupil area is 15% of the total beam area, the axial FWHM is increased by 26%. When the pupil area is increased to 25% of the total beam area, elongation along the axial dimension is increased by 43%. These calculations confirm that central obscuration of the beam significantly affects confinement along the axial coordinate.

We note that a maximum NA of up to 1.33 for water-dipped samples is, in principle, possible by either increasing the mirror diameter or further decreasing the focal length of the parabolic mirror.

#209910 - $15.00 USD Received 9 Apr 2014; revised 21 May 2014; accepted 21 May 2014; published 9 Jun 2014

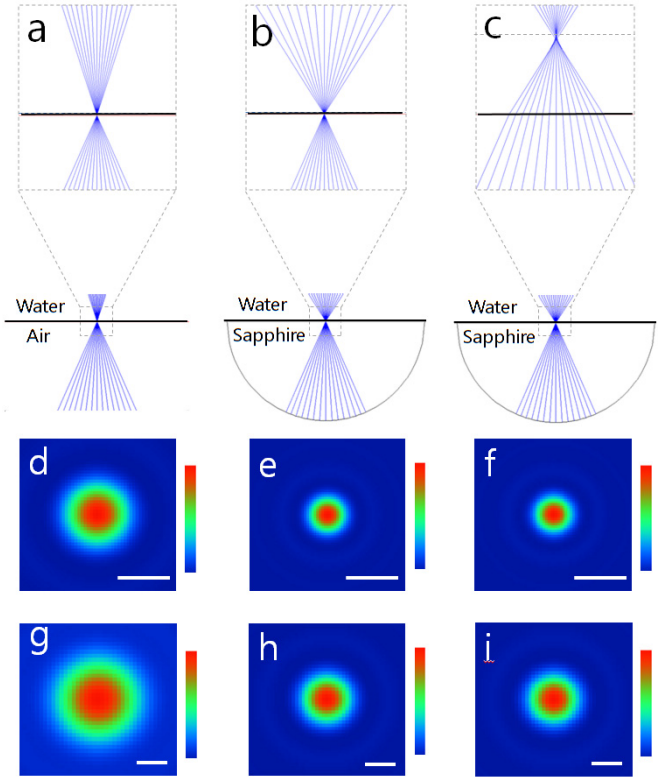

Fig. 2. Ray tracing and PSF calculation results of solid immersion VR-SFG microscopy. Traced rays from the parabolic mirror (a) without SIL and (b),(c) with SIL. (c) represents the situation that the laser beam focuses 10 μm deep into the water medium. The ray tracing is performed at 775 nm. Focal spot intensity distributions of the corresponding cases calculated (d),(e),(f) at 775 nm and (g),(h),(i) at 3.4 μm. The scale bars are (d),(e),(f) 1 μm and (g),(h),(i) 2 μm. The ray tracings at 3.4 μm are not presented here due to the similarity with those at 775 nm. It is noticeable that no appreciable aberration is induced even though the laser beams focus far beyond the SIL surface.

4. Experimental results and discussion

To test the imaging performance and measure the spatial resolution of solid immersion VR-SFG microscopy, we use 0.30 μm diameter barium titanate ($BaTiO_3$) nano-particles as the imaging target. $BaTiO_3$ exhibits a high second-order nonlinear susceptibility $\chi^{(2)}$, and produces a strong nonresonant SFG signal. The sample is prepared directly on the flat SIL surface. Without polarization adjustment, we obtain the imaging result as shown in Fig. 3(a). It clearly shows duplicate images of nano-particles aggregates as indicated by the pairs of white arrows. This effect results from the birefringence of the sapphire SIL, which generates two focal spots corresponding to two different polarization states of the incident laser beams. It can be seen from Fig. 3(a) that the two duplicate images show slightly different shapes, possibly because the $BaTiO_3$ nano-particles may respond differently to different polarizations. Next we rotate the incident linear polarization to select for one dominant (linear) polarization state at the sample, producing the image shown in Fig. 3(b). This confirms that proper care of the polarization state of the incident light is required when using birefringent SILs for optical microscopy applications.

#209910 - $15.00 USD Received 9 Apr 2014; revised 21 May 2014; accepted 21 May 2014; published 9 Jun 2014

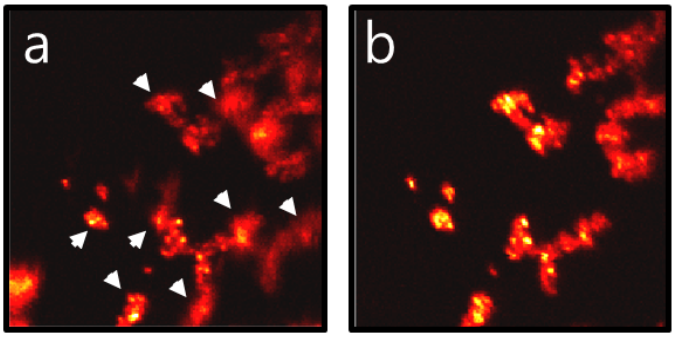

Fig. 3. Solid immersion VR-SFG images of barium titanate nano-particles aggregates. The single particle size is 300 nm. Due to the birefringence of sapphire, two duplicated images appeared as in (a) if measured in arbitrary polarization direction. After properly aligning the incident polarization, only a single image was obtained as in (b). The fields of view (FOV) are 60 μm x 60 μm. Notice the bright image in the bottom-left corner of (a), which falls outside the FOV of (b).

We next focus on a single nano-particle to determine the spatial resolution, by raster scanning the target through focus. Note that the actual scanning range of the piezo translation stage is 1.76 times larger than the recorded image area. This is due to the fact that the SIL physically moves with the sample and acts as a de-magnifier with the magnification ratio $1/n_{sapphire}$ for the incoming beam [19]. From the imaging results shown in Fig. 4(b), we observe that the spot size is much reduced compared to the image measured without the sapphire SIL (Fig. 4(a)). Comparing the intensity profiles across the two spot images, we find that the PSF is reduced by a factor of 1.72 from 1.1 μm to 0.64 μm, very close to the theoretical value of 1.76. Because the MIR focal spot size is much bigger than the NIR spot size as shown in Fig. 2(g)-2(i), the spatial resolution of VR-SFG microscopy is predominantly governed by the NIR focal spot. Due to the absence of a central obscuration in the off-axis parabolic objective mirror, an annular focal pattern that is typical for Schwarzschild reflective lenses [5,6], is not observed here. The inset in Fig. 4(a) shows the focal spot shape (not scaled) encountered when the confocality of the two parabolic mirrors in the beam expanding telescope is lifted to a 3~4 mm mismatch, showing severe coma-shaped aberrations.

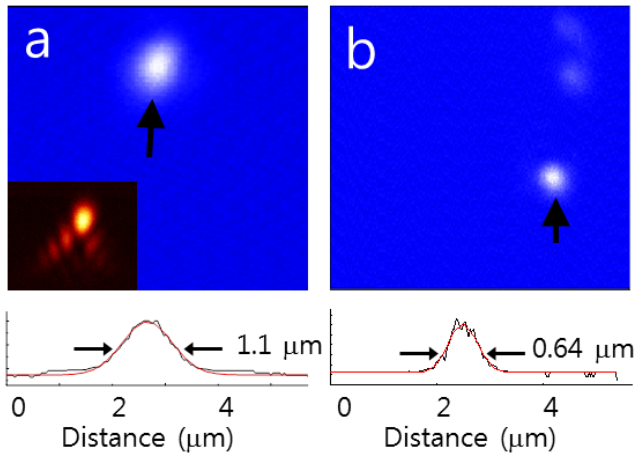

Fig. 4. Point spread function measurement results of VR-SFG microscopy (a) without SIL and (b) with SIL. A single nano-particle of barium titanate was raster-scanned across the focal spot for each case. It is clearly shown that the system NA is enhanced by the sapphire SIL, close to a factor of $n_{sapphire}$. The red curves are Gaussian fits to the measured data. The inset in (a) shows the focal spot shape (not scaled) encountered when the confocality of two parabolic mirrors in the beam expanding telescope is slightly broken. The fields of view are 11.4 μm x 11.4 μm for both images.

#209910 - $15.00 USD Received 9 Apr 2014; revised 21 May 2014; accepted 21 May 2014; published 9 Jun 2014

Finally we apply the solid immersion VR-SFG microscope to imaging collagen fibers in rat tail tendons and hawk cornea. The MIR wavelength is tuned to the 2945 cm^{-1} resonance of the methylene modes in collagen. The tissue samples are put directly on top of the flat SIL surface. A drop of water is used for immersion, and the sample is covered with a glass coverslip. The power levels of the parallel polarized NIR and MIR beams are 16 mW and 5 mW at 775 nm and 3.4 μm, respectively, as measured before the SIL. In Fig. 5, VR-SFG images are shown for the situation with (5b, d) and without (Fig. 5(a), 5(c)), the sapphire SIL. The total acquisition time for each image was 1 minute for an image with 256 × 256 pixels, primarily limited by the scan speed of the piezo translation stage rather than the magnitude of the VR-SFG signal. In general, we observe that the images obtained with the SIL show finer collagen structures and more details compared to the images without the SIL. The more pronounced details are a direct consequence of the improved lateral resolution provided by the solid immersion.

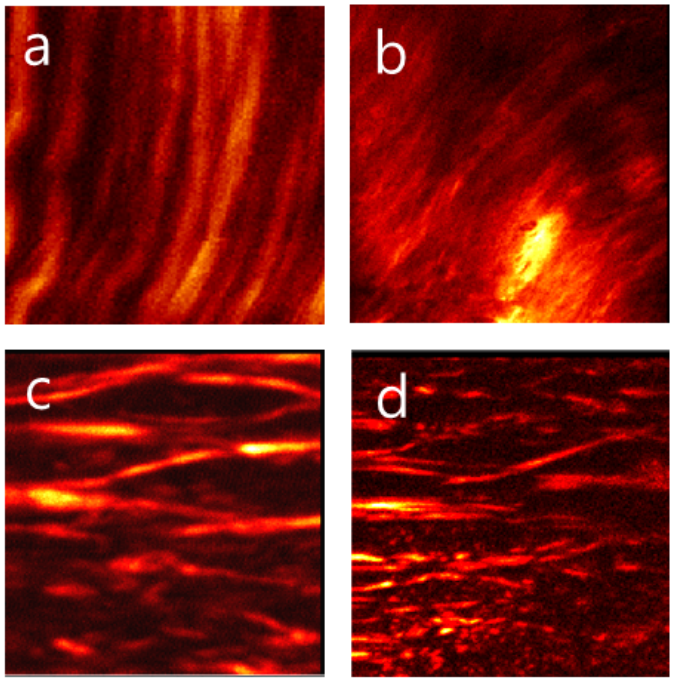

Fig. 5. (b),(d) Solid immersion VR-SFG microscopic images of biological samples compared to (a),(c) the corresponding images measured without SIL. (a),(b) Rat tail tendon collagen and (c),(d) hawk cornea collagen. The fields of view are 80 μm x 80 μm. The power levels of the parallel polarized NIR and MIR beams were 16 mW and 5 mW at 775 nm and 3.4 μm, respectively.

Compared to previous implementations of VR-SFG microscopy, the approach presented here has several important advantages. First, the use of an all-reflective telescope and focusing mirror represents a simple yet effective method for generating the dual-color VR-SFG excitation volume. Reflective optics minimize chromatic aberrations, which is especially important when focusing NIR and MIR light to the same focal spot in a collinear fashion. Second, off-axis parabolic mirrors enable focusing without the central obscuration that is inherent to Schwarzschild focusing optics. The clear aperture enables the formation of a clean focus, with minimum diffraction side lobes. Importantly, the elongated focus characteristic of Schwarzschild focusing is absent in the current approach, allowing signal generation from an excitation volume that is more confined in the axial dimension. Using off-the-shelf parabolic mirrors, we readily achieve VR-SFG imaging with an effective NA of 0.42. Third, the use of a hemispheric sapphire solid immersion lens significantly improves the resolution of the

#209910 - $15.00 USD Received 9 Apr 2014; revised 21 May 2014; accepted 21 May 2014; published 9 Jun 2014

focusing system. Sapphire exhibits excellent transparency and a high refractive index over a wide spectral range from the ultraviolet to the mid-infrared (more than 80% transmission in the 400 nm to 3.5 μm window). Our theoretical analysis indicates that the chromatic aberrations introduced by the sapphire material are small compared to the axial resolution. Our experiments indicate that clean and confined SFG excitation volumes can be produced with the SIL, giving rise to a lateral resolution improvement by a factor of 1.72, in close agreement with the theoretically predicted value. Using this inexpensive configuration, we achieve VR-SFG imaging of biological samples with a resolution of 0.64 μm.

Although this performance rivals the lateral resolution attained with commercial Schwarzschild objectives, it is important to underline that the images obtained with SIL focusing are not distorted by side lobes of the PSF and that the axial extent of the focal volume is markedly reduced. Our calculations show an axial resolution of 3.5 μm, which is significantly higher than what can be theoretically obtained with Schwarzschild-type lenses. Even though the current mounted SIL configuration prevents us from performing an axial scan to experimentally verify the axial resolution, it is clear from focal volume simulations that the absence of the center obscuration significantly improves the confinement along the axial dimension.

An important shortcoming of the current implementation is the fact that the SIL is mounted directly to the sample. In this configuration, the optical axis of the SIL is continuously displaced relative to optical axis of the system while scanning the translation stage. As the SIL axis moves away from the system axis, aberrations are introduced, which consequently limit the extent of the field-of-view (FOV). The effective FOV is a function of wavelength, lens diameter, incident NA, and refractive index of the SIL [28]. A larger SIL provides a larger FOV. In our case, the diameter of the FOV is as large as 140 μm, much larger than the FOV of the images presented here. However, this limited area eventually makes it difficult to access different regions in the sample as the lens is mounted directly to the specimen. To solve this problem, we are currently considering a new design of the SIL that is composed of two elements, consisting of a thin plan-parallel plate and a thick planar convex spherical lens. The combined thickness of two pieces can be manufactured to match the radius of the original SIL. The sample is then positioned on the plate, while sliding over the flat surface of the lens, with the lens axis fixed while scanning.

Although sapphire is a hard material with a high refractive index, its birefringence complicates the alignment procedure. Other high refractive index materials that are optically isotropic, such as ZnSe, would simplify the alignment of the microscope. Future studies will focus on finding alternative materials for the solid immersion lens to improve the imaging properties of the microscope.

Because of the vast chromatic shifts between the excitations wavelengths, achieving high-resolution VR-SFG is a challenge. In this work, we show that some of these challenges can be overcome with relatively inexpensive focusing optics. The combination of an off-axis parabolic mirror and a sapphire SIL yields a lateral resolution of 0.64 μm, with a higher degree of 3D confinement than what was previously obtained with Schwarzschild objectives. Improving the lateral resolution further is relatively straightforward by increasing the aperture of the off-axis parabolic mirror. The possibility to reach higher resolution in VR-SFG with off-the-shelf optical components is significant, as it avoids the need for expensive, custom-designed reflective objectives, thus opening up the way for further development of VR-SFG microscopy into a practical high-resolution imaging technique.

5. Conclusion

We demonstrate high spatial resolution solid immersion VR-SFG microscopy in the MIR region by combining an off-axis parabolic mirror and a hemispheric sapphire SIL. Using the parabolic mirror as an objective lens, the central obscuration inherent to Schwarzschild objectives can be avoided, producing clean diffraction-limited focal volumes. The implementation of a sapphire solid immersion lens improved the effective NA of 0.42 to NA 0.72, in close agreement with theory. This focusing configuration can be extended to design

#209910 - $15.00 USD Received 9 Apr 2014; revised 21 May 2014; accepted 21 May 2014; published 9 Jun 2014

NAs of up to 1.33 in aqueous media, without relying on evanescent near-field effects. We show that this simple and inexpensive focusing system is suitable for generating high quality VR-SFG images in biological samples such as rat tail tendon and hawk cornea.

Acknowledgment

We thank Prof. James Jester for providing the hawk cornea sample. We acknowledge support from Bio-signal Analysis Technology Innovation Program funded by the Ministry of Science, ICT and Future Planning, Republic of Korea. E. O. Potma is grateful for the support from NSF grant CHE-0847097, and NIH grant P41-RR01192 (Laser Microbeam and Medical Program, LAMMP). JH acknowledges support from the NSF IGERT program in biophotonics at UCI (NSF-DGE-1144901).

#209910 - $15.00 USD Received 9 Apr 2014; revised 21 May 2014; accepted 21 May 2014; published 9 Jun 2014